



Provided by the author(s) and University of Galway in accordance with publisher policies. Please cite the published version when available.

Title	Application of the meshless finite volume particle method to flow-induced motion of a rigid body
Author(s)	Nestor, Ruairi M.; Quinlan, Nathan J.
Publication Date	2013-10-01
Publication Information	Ruairi M. Nestor, Nathan J. Quinlan (2013) 'Application of the meshless finite volume particle method to flow-induced motion of a rigid body'. Computers & Fluids, .
Publisher	ScienceDirect
Link to publisher's version	<a href="http://dx.doi.org/10.1016/j.compfluid.2013.10.004">http://dx.doi.org/10.1016/j.compfluid.2013.10.004</a>
Item record	<a href="http://hdl.handle.net/10379/4023">http://hdl.handle.net/10379/4023</a>
DOI	<a href="http://dx.doi.org/10.1016/j.compfluid.2013.10.004">http://dx.doi.org/10.1016/j.compfluid.2013.10.004</a>

Downloaded 2024-03-20T10:22:41Z

Some rights reserved. For more information, please see the item record link above.



Preprint of

# Application of the meshless finite volume particle method to flow-induced motion of a rigid body

Ruairi M. Nestor and Nathan J. Quinlan

Computers and Fluids

2013

[DOI: 10.1016/j.compfluid.2013.10.004](https://doi.org/10.1016/j.compfluid.2013.10.004)



National University of Ireland, Galway

# Application of the meshless finite volume particle method to flow-induced motion of a rigid body

R. M. Nestor<sup>1</sup>, N. J. Quinlan\*

*Mechanical and Biomedical Engineering, College of Engineering and Informatics, National University of Ireland Galway, Ireland*

---

## Abstract

We present a new approach to numerical modelling of incompressible flow of fluid about an elastically mounted rigid structure with large body motions. The solution is based on the Finite Volume Particle Method (FVPM), a meshless generalisation of the mesh-based finite volume method. The finite volume particles are allowed to overlap, without explicit connectivity, and can therefore move arbitrarily to follow the motion of a wall. Here, FVPM is employed with a pressure projection method for fully incompressible flow coupled with motion of a rigid body. The developed extension is validated for Vortex-Induced Vibration (VIV) of a circular cylinder in laminar crossflow. To minimise computational effort, non-uniform particle size and arbitrary Lagrangian-Eulerian particle motion schemes are employed, with radial basis functions used to define the particle motion near the cylinder. Close agreement is demonstrated between the FVPM results and a reference numerical solution. Results confirm the feasibility of FVPM as a new approach to the modelling of flow with strongly coupled rigid-body dynamics.

*Key words:* particle, meshless, finite volume particle method, vortex-induced vibration, fluid-structure interaction

---

---

\*Corresponding author

<sup>1</sup>Current address: MCS Kenny, Parkmore, Galway, Ireland

## 1. Introduction

Many important problems in fluid dynamics are dominated by moving boundaries. Examples include the heart and blood vessels, internal combustion engines, animal flight and vortex-induced vibration of slender elastic structures. In classical computational fluid dynamics based on boundary-conforming meshes, special treatments (such as mesh deformation, remeshing, overset meshes and immersed boundaries) are required for flows of this kind. In meshless methods, in contrast, the computational nodes or particles are free to move in response to boundary motions, since their connectivity need never be specified. Therefore, it appears that meshless methods can avoid the difficulties presented by a mesh with moving boundaries.

There is now a significant body of work on the meshless method smoothed particle hydrodynamics (SPH) demonstrating validated applications in a range of applications, notably in free-surface flow. SPH was first applied to free-surface flow by Monaghan [1] using a weakly compressible approach. Incompressible free-surface SPH methods were developed by Cummins and Rudman [2] using a pressure projection, and by Shao and Lo using a density-invariant formulation [3]. A comprehensive review is given by Monaghan [4].

The relatively new finite volume particle method (FVPM) is a meshless generalisation of the classical mesh-based finite volume method which, in principle, avoids some limitations of other meshless methods. The central idea of FVPM, and the main difference between it and the mesh-based finite volume method, is the definition of an interface area between overlapping finite volume cells (particles), in contrast with the contiguous but strictly non-overlapping finite volume cells in a mesh. Since finite volume particles may overlap arbitrarily, there is no need to determine or maintain connectivity information. They can move in any manner, as long as fluxes due to the particles' motion are accounted for. This makes it straightforward to accommodate moving boundaries. Where a particle is truncated by a boundary, a particle-boundary interface area is defined, enabling boundary flux to be computed. FVPM was introduced by

Hietel *et al.* [5]. It was subsequently analysed by Junk and Struckmeier [6] and Junk [7], proving consistency of the scheme, and rigorously establishing FVPM as a generalisation of the finite volume method. Keck *et al.* [8] implemented a pressure projection scheme for fully incompressible flow. Improved methods for the particle interface area calculation were proposed by Hietel and Keck [9] and Teleaga [10]. Nestor *et al.* [11] extended FVPM to second-order spatial accuracy and viscous flows, and Teleaga [10, 12] and Nestor *et al.* [13] applied the method to moving-boundary problems.

FVPM embodies some valuable properties of the finite volume method without sacrificing the flexibility of a meshless method for moving boundaries and interfaces. Boundary conditions are implemented straightforwardly by prescription of fluxes from the boundary to the particle. FVPM possesses proven theoretical consistency [6], and local conservation is exact, regardless of variation in particle size. In addition, a wide range of established finite volume techniques (e.g. Riemann solvers) can be directly incorporated in FVPM. However, there have been few applications of FVPM to date, and most have been restricted to simple benchmark problems.

This article is concerned with development and validation of FVPM for a more challenging problem in which full advantage can be taken of the meshless formulation. We describe the extension of the FVPM to flow-induced motion of a rigid structure (henceforth referred to as rigid-body FSI) for incompressible flow. This extension is validated for Vortex-Induced Vibration (VIV) of a circular cylinder in cross-flow, a problem involving coupling of fluid dynamics with a rigid body undergoing large displacements. The motivation for this study is to validate FVPM on a well-studied fluid-structure interaction problem, in advance of applications involving more complex rigid-body dynamics and/or elastic bodies.

The FVPM formulation is described in Section 2. The rigid-body FSI extension of FVPM is presented in Section 3 and a novel ALE particle motion scheme for FVPM is presented in Section 4. Results are presented in Section 5 from FVPM simulations for crossflow over a circular cylinder vibrating with pre-

scribed motion and a freely vibrating cylinder. The FVPM results are compared with reference solutions from the literature throughout.

## 2. The Finite Volume Particle Method

### 2.1. FVPM formulation

The semi-discrete form of the FVPM for a conservation law is [5, 12]

$$\frac{d}{dt}(V_i \mathbf{U}_i) = - \sum_{j=1}^N \beta_{ij} (\mathcal{F}(\mathbf{U}_i, \mathbf{U}_j)) - \beta_i^b \mathcal{F}_i^b, \quad (1)$$

where  $t$  is time,  $V_i$  is the volume of particle  $i$ , and  $\mathbf{U}$  is the vector of conserved variables. The numerical flux  $\mathcal{F}(\mathbf{U}_i, \mathbf{U}_j)$  is an approximation to  $\mathbf{F}_{ij} - \bar{\mathbf{U}}_{ij} \bar{\mathbf{x}}_{ij}$ , where  $\bar{\mathbf{U}}_{ij}$  and  $\bar{\mathbf{x}}_{ij}$  are averages of the conserved variables and particle transport velocity, respectively, of particle  $i$  and its neighbour  $j$ . The superscript  $b$  denotes boundary terms. The element of FVPM which differentiates it from the classical finite volume method is the particle interaction vector, defined by

$$\beta_{ij} = \int_{\Omega} \frac{W_i \nabla W_j - W_j \nabla W_i}{(\sum_k W_k)^2} d\mathbf{x}, \quad (2)$$

where  $W_i = W(\mathbf{x} - \mathbf{x}_i(t), h)$  is a compactly supported kernel function for particle  $i$ , centred at  $\mathbf{x}_i$ . The compact support radius is  $2h$ , where  $h$  is called the smoothing length, in keeping with the SPH convention. The quantity  $\beta_{ij}$  is precisely analogous to the cell face normal area vector which weights intercell fluxes in the classical finite volume method [7]. The particle interaction vectors are evaluated by numerical integration and corrected by the procedure of Teleaga [10] to ensure the condition  $\sum_j \beta_{ij} = 0$  (analogous to the condition that a cell surface is closed in traditional finite volume methods) is exactly satisfied.

Interparticle fluxes are computed using a MUSCL reconstruction from particle barycentres to particle-particle interfaces, as described by Nestor *et al.* [11]. The reconstruction is based on a consistency-corrected SPH estimate of gradients [14] at the particle barycentre. The HLL Riemann solver [15] is then used to approximate the interparticle inviscid momentum fluxes.

One valuable property of FVPM, exploited in the present work, is that particle size may be spatially non-uniform. That is, neighbours  $i$  and  $j$  can have different support radius  $2h$ . In the form used here,  $h_i$  is constant in time, although the case  $h = h(t)$  may also be treated with an additional term involving  $dh/dt$  [5]. A second-order explicit Runge-Kutta scheme is used for temporal discretisation of Eq. (1).

For full details of FVPM, the reader is referred to Hietel *et al.* [5]. The implementation in the present work follows the details given by Nestor *et al.* [11, 13], except where stated otherwise.

## 2.2. Fully incompressible solution methodology

FVPM has previously been applied to fully incompressible flow problems by several authors [8, 13, 16]. The pressure projection algorithm of Chorin [17], adapted for SPH by Cummins and Rudman [2], is used to achieve the fully-incompressible flow solution. The algorithm can be summarised (using a first-order explicit temporal discretisation for brevity) by the following sequence of steps:

$$V_i^{n+1} = V_i^n + \Delta t \frac{dV_i^n}{dt} \quad (3)$$

$$\mathbf{U}_i^* = \frac{1}{V_i^{n+1}} \left( V_i^n \mathbf{U}_i^n + \Delta t \frac{d(V_i \mathbf{U}_i)^{*,n}}{dt} \right) \quad (4)$$

$$\mathbf{x}_i^{n+1} = \mathbf{x}_i^n + \Delta t \dot{\mathbf{x}}_i^n \quad (5)$$

$$\nabla^2 p_i^{n+1} = \frac{\rho}{\Delta t} \nabla \cdot \mathbf{u}_i^* \quad (6)$$

$$\mathbf{u}_i^{n+1} = \mathbf{u}_i^* - \frac{\Delta t}{\rho} \nabla p_i^{n+1} \quad (7)$$

where  $d(V_i \mathbf{U}_i)^{*,n}/dt$  is computed from Eq. (1) without the pressure term in the flux function  $\mathcal{F}$ . The algorithm consists of a preliminary time advance of the momentum equation (disregarding the pressure terms) which yields the momentum  $\mathbf{U}^*$  in Eq. (4) that is not guaranteed to satisfy the divergence-free velocity condition. The pressure solution at time  $n + 1$  is computed in Eq. (6). The velocity is corrected in Eq. (7) so that the divergence-free velocity condition is satisfied.

Care must be taken when developing the discrete form of the pressure Poisson equation (Eq. 6) to ensure that the discrete scheme does not admit spurious checkerboard solutions for the pressure. An appropriate choice for the discrete Laplacian and divergence operators is described by Nestor and Quinlan [13].

In the present work, the solution to the discretised pressure Poisson equation in Eq. (6) is obtained with the LASPACK implementation of the GMRES algorithm [18].

### 2.3. Boundary conditions

A significant advantage of FVPM over other mesh-free methods is that boundary fluxes can be prescribed straightforwardly wherever a particle is truncated by a boundary. The discretisation of these terms allows for a straightforward enforcement of boundary conditions in terms of a boundary flux and a geometric interaction vector. Following Keck [16] and Keck and Hietel [8], the boundary coefficient  $\beta_i^b$  in Eq. (1) may be computed from

$$\beta_i^b = - \sum_{j=1}^N \beta_{ij}. \quad (8)$$

Specific boundary conditions are then applied by prescribing the appropriate flux  $\mathcal{F}_i^b$  where a particle is truncated by a boundary. For inlet, no-slip wall and free-slip wall boundaries, the normal component of velocity is specified. The inviscid flux at the boundary is then computed on the basis of the imposed boundary velocities and a zero-order extrapolation of the particle pressure to the boundary. At no-slip wall boundaries, the viscous fluxes are computed on the basis of a consistency-corrected SPH gradient approximation [14], centred at the midpoint of the boundary segment that overlaps the particle support. For free-slip walls, the viscous flux is set to zero.

For the pressure Poisson equation, a Neumann condition  $\nabla p_i^b = \mu \nabla^2 \mathbf{u}_i^b$  is specified at inlet and no-slip wall boundaries. At free-slip wall boundaries, a homogeneous Neumann condition is specified.

For outlet boundary conditions, following the approach of Ferziger and Peric [19], the velocity gradient normal to the boundary is set to zero, and the resulting



outlet mass fluxes are corrected so maintain global mass conservation. For the pressure Poisson equation, the pressure is specified at the outlet.

### 3. Rigid-body FSI in the FVPM

#### 3.1. Equation of motion for the rigid structure

In the VIV simulations presented in Section 5.3, a rigid structure of mass  $m$  and length scale  $d$  is mounted on springs with stiffness  $k$  in each Cartesian coordinate direction, without damping, and is immersed in a flow. The structure is subjected to a total fluid force  $\mathbf{F}_f$  comprising viscous and pressure components. The equation of motion for the structure is written as

$$\ddot{\mathbf{x}}_c + 4\pi^2 f_n^2 \mathbf{x}_c = \frac{\mathbf{F}_f}{M^* \rho d^2}, \quad (9)$$

where  $\mathbf{x}_c$  is the structure displacement vector relative to the no-flow equilibrium position,  $f_n = \sqrt{k/m}/(2\pi)$  is the undamped natural frequency of the system and  $M^* = m/(\rho d^2)$  is the non-dimensionalised mass.

The components of surface force on the cylinder are approximated in FVPM by

$$F_x \approx \sum_i |\beta_i^b| (p_i^b n_x - n_y \tau_i^b), \quad (10)$$

where  $n_x$  is the  $x$ -component of the outward (away from the fluid domain) normal at the cylinder surface, and the sum includes all particles  $i$  interacting with the cylinder. The boundary pressure is extrapolated to the boundary *i.e.*  $p_i^b = p_i$ , and the boundary viscous stress  $\tau_i^b$  is computed using the SPH gradient approximations.

#### 3.2. Algorithm for fluid-structure coupling

The structure position at time level  $n+1$  is approximated using the equation of motion for the structure and the fluid forces acting on the structure at time level  $n$ . A staggered approach [20–22] is chosen for fluid-structure coupling. In the following, the method is described for a first-order explicit temporal scheme for simplicity, although a second-order Runge-Kutta scheme is employed in our

implementation. The position and velocity of the structure are firstly updated to time level  $n + 1$ . The computational mesh (particle distribution, in the case of FVPM) is then updated to account for the displaced structure. Finally, the flow field is updated to time level  $n + 1$ . The details of the implementation follow the work of Placzek *et al.* [22], and is detailed in Algorithm 1.

Throughout this article, to appropriately move the particles in the vicinity of a moving boundary, the motion of these particles is computed on the basis of an interpolation of the boundary motion velocities using the procedure described in Section 4. Using this approach, the particle velocity at timestep  $n + 1$  (*i.e.*  $\dot{\mathbf{x}}_i^{n+1}$  in step 6 of Algorithm 1), is based on the boundary velocity at the same timestep (*i.e.*  $\dot{\mathbf{x}}_c^{n+1}$  in step 3 of Algorithm 1). Therefore, the boundary and particle positions are updated using the same temporal scheme. This differs from the approach of Placzek *et al.* [22] in which the updated structure position is based on an average of both the previous and current structure velocities, *i.e.*  $\mathbf{x}_c^{n+1} = \mathbf{x}_c^n + (\Delta t/2) (\dot{\mathbf{x}}_c^n + \dot{\mathbf{x}}_c^{n+1})$ . However, the current approach has been found to perform well for the test cases presented in Section 5.3.

#### 4. Particle Motion

In FVPM, particles are transported with an arbitrary Lagrangian-Eulerian (ALE) velocity field. For application to VIV simulation, a fully Eulerian scheme cannot be used, because of the cylinder wall motion. A fully Lagrangian scheme would be computationally expensive because of the need to recompute particle neighbourhoods and interactions at every timestep. Therefore, a hybrid ALE approach is used, in which particles far from the vibrating cylinder remain stationary (Eulerian), and particles near the moving walls are transported at a velocity based on interpolation of the wall velocity. Radial basis functions (RBF) are used for interpolation, following de Boer *et al.* [23], but with interpolation for particle velocities rather than displacements, since particle velocity is required in FVPM for the computation of the interparticle fluxes.

Given a set of  $n$  discrete data points  $\mathbf{x}_j$ ,  $j = 1 \dots n$  at which the scalar

function  $s(\mathbf{x})$  is known, a RBF interpolation  $\tilde{s}(\mathbf{x})$  for  $s(\mathbf{x})$  may be written as

$$\tilde{s}(\mathbf{x}) = \sum_{j=1}^n \alpha_j \Phi(|\mathbf{x} - \mathbf{x}_j|) + p(\mathbf{x}), \quad (11)$$

where  $\Phi$  is a radial basis function centred at  $\mathbf{x}_j$ ,  $p$  is a polynomial, and  $\alpha$  is a vector of coefficients with a single  $\alpha_j$  for each data point  $\mathbf{x}_j$ . For FVPM, the known data points  $\mathbf{x}_j$  are points on the boundaries which move with known velocity.  $\Phi$  is a radially symmetric function, certain choices for which have compact support. According to Buhmann [24], the purpose of the polynomial  $p$  in Eq. (11) is to ensure that the interpolation problem is non-singular for certain choices of  $\Phi$ . The coefficients  $\alpha_j$  and the coefficients of the polynomial  $p$  can be obtained by requiring that two conditions on the interpolation are satisfied. The first condition is that the known data are recovered by the interpolation Eq. (11) at the discrete data points,

$$\tilde{s}(\mathbf{x}_j) = s(\mathbf{x}_j). \quad (12)$$

The second condition is

$$\sum_{j=1}^n \alpha_j p(\mathbf{x}_j) = 0, \quad (13)$$

which, according to Buhmann [24], is required to ensure that the interpolant is unique.

In the present work, we follow de Boer *et al.* [23] in that a first-order polynomial is used for  $p$ . The present choice for  $\Phi$  is the compactly supported polynomial

$$\Phi(|\mathbf{x} - \mathbf{x}_j|, q) = \begin{cases} \left(4\frac{|\mathbf{x} - \mathbf{x}_j|}{q} + 1\right) \left(1 - \frac{|\mathbf{x} - \mathbf{x}_j|}{q}\right)^4 & \text{if } \frac{|\mathbf{x} - \mathbf{x}_j|}{q} < 1 \\ 0 & \text{otherwise} \end{cases}, \quad (14)$$

where  $q$  is the compact support radius of  $\Phi$ . The compact support radius  $q$  is typically of the order of the maximum dimension of the domain. The choice for  $\Phi$  given in Eq. (14) was shown by de Boer *et al.* [23] to require the least computational effort of several choices for  $\Phi$ .

Denoting as  $\Theta$  the vector of coefficients of the polynomial  $p$ , the solution for  $\alpha$  and  $\Theta$  can be obtained by solving the linear system

$$\begin{bmatrix} \mathbf{M} & \mathbf{P} \\ \mathbf{P}^T & \mathbf{0} \end{bmatrix} \begin{bmatrix} \alpha \\ \Theta \end{bmatrix} = \begin{bmatrix} \mathbf{s} \\ \mathbf{0} \end{bmatrix}, \quad (15)$$

where the submatrix  $\mathbf{M}$  has dimensions  $n \times n$  with  $\mathbf{M}_{ij} = \Phi(|\mathbf{x}_i - \mathbf{x}_j|)$ ,  $\mathbf{P}$  is a  $n \times (D + 1)$  submatrix, with row  $j$  of  $\mathbf{P}$  given by  $\mathbf{P}_j = [1 \quad \mathbf{x}_j]$  and  $\mathbf{s}$  is a vector of dimension  $n$  with  $\mathbf{s}_j = s(\mathbf{x}_j)$ . The solution to Eq. (15) is obtained using the LSPACK implementation [18] of the Generalised Minimal Residual Method (GMRES) [25].

## 5. Numerical results

Example computations of the developed methods are presented in this section. Vortex-induced vibration (VIV) of circular cylinders in crossflow is overviewed in 5.1. Simulations of flow around a cylinder undergoing prescribed vibrations are then presented in Section 5.2. The purpose of these simulations is to verify that the forces acting on the structure predicted by the FVPM are in agreement with similar computations in the literature. The extension of the FVPM for rigid-body FSI is then validated in Section 5.3 for VIV of a circular cylinder in crossflow.

### 5.1. Overview of vortex-induced vibration of cylinders in crossflow

VIV [26] is an important consideration for the design of long elastic structures such as offshore risers [27] and skyscrapers [28]. VIV of an elastically mounted cylinder in laminar crossflow has been extensively studied both experimentally and numerically. This case is chosen as the subject of the present work for validation of rigid-body FSI modelling in FVPM. Comprehensive reviews of VIV are presented by Bearman [26], Williamson and Govardhan [29] and Sarpkaya [30].

The VIV response of an elastically-mounted circular cylinder of diameter  $d$  is illustrated in Figures 1(a) and 1(b) for a range of reduced velocity

$U_r = U_\infty/(f_n d)$ . Within the lock-in range, the cylinder displacement amplitude is higher, and the vortex shedding and cylinder motion synchronise with the natural frequency of the structure  $f_n$ . Outside of this range of  $U_r$ , the cylinder motion is synchronised with the Strouhal frequency  $f_s$  and the cylinder displacement amplitude is small.

The structure of the VIV response is dependent on structural parameters and flow conditions. The upper branch of amplitude response (illustrated in Figure 1) does not occur for laminar flow, as demonstrated by the numerical simulations of Newman and Karniadakis [31] and the experimental observations of Anagnostopoulos and Bearman [32]. The experiments of Khalak and Williamson [33] show that the synchronisation of the cylinder vibration frequency  $f_c$  with the natural frequency  $f_n$  is not as well defined for small  $M^*$  as for large  $M^*$ , as illustrated in the schematic plot in Figure 1(b). Measurements by Anagnostopoulos and Bearman [32] show that the long-term amplitude response is sensitive to initial conditions. The authors performed two sets of experiments in which the cylinder response was observed as a function of  $U_r$ . Their findings are illustrated schematically in Figure 1(a). If the cylinder is stationary in the initial condition (referred to as “starting from rest” or the “stationary initial condition” in this article), lock-in occurs over a smaller range of  $U_r$  than if  $U_r$  is increased over the course of the experiment, allowing periodic VIV to become established before advancing to the next condition.

Williamson and Roshko [34] have identified several vortex shedding modes that occur for flow over vibrating circular cylinders, as shown schematically in Figure 2. In the 2S and 2P modes, respectively, two single vortices and two pairs of vortices are shed per cylinder motion cycle. In the P+S mode, in which one single and one pair of vortices are shed per cycle, and in the C(2S) mode, vortices coalesce in the wake. For laminar flow, the 2P wake mode has not been observed in the forced vibration experiments of Griffin and Ramberg [35] at  $Re_d = 190$  or the numerical simulations of Singh and Mittal [36] and Prasanth and Mittal [37] at  $Re_d = 100$  and  $60 < Re_d < 200$  respectively. Instead, the predominant vortex mode for laminar VIV is the 2S mode. In the computations

of Singh and Mittal [36] at  $Re_d = 100$ , the C(2S) mode occurs for  $U_r = 5.0$  (with increasing  $U_r$ ) and  $U_r = 4.6$  (with decreasing  $U_r$ ).

In numerical simulations of undamped VIV at low Reynolds number, Shiels *et al.*[38] found that the effects of structural stiffness and mass can be characterised by a single effective stiffness parameter which is valid even for zero mass and stiffness. Williamson and Govardhan [29] compiled low Reynolds number results from the experiments of Anagnostopoulos and Bearman [32] and a range of numerical models, to showing that amplitude response as a function of oscillation frequency is essentially independent of  $M^*$  and  $Re_d$  for  $0 \leq M^* \leq 116$  and  $Re_d \leq 200$ .

## 5.2. Forced vibrations of a cylinder in crossflow

Laminar flow over a circular cylinder vibrating with prescribed motion is simulated as a precursor to VIV simulation. The lock-in phenomenon associated with VIV also occurs for forced cylinder vibrations — in the forced case, lock-in is characterised by the synchronisation of the vortex shedding and cylinder vibration for a certain range of cylinder vibration frequency  $f_c$ . Outside of this range, this synchronisation is not observed. Thus, this flow problem tests the ability of the FVPM to predict some VIV-related flow phenomena without the need to model the structural response.

The numerical simulations of Placzek *et al.*[22] are used for comparison with the FVPM results. Their simulations are based on a mesh-based finite volume discretisation with a second-order upwind approximation for the inter-volume fluxes. For their forced vibration simulations, Placzek *et al.*[22] used a 2D mesh of 28,800 quadrilateral elements.

### 5.2.1. Problem definition

The problem domain is illustrated schematically in Figure 3. An inlet boundary condition with specified normal velocity of  $U_\infty$  is located at  $x^* = x/d = 0$ . Free-slip horizontal wall boundary conditions are located at  $y^* = y/d = \pm 15$ . An outlet boundary condition with prescribed pressure  $p = 0$  is located at

$x^* = 80$ . The flow is laminar with Reynolds number  $Re_d = 100$ . The cylinder moves in the  $y$ -direction only with position  $y_c(t)$  given by

$$y_c(t) = A \sin(2\pi f_c t), \quad (16)$$

where  $A$  is the amplitude of the motion and  $f_c$  is the cylinder vibration frequency.

The imposed cylinder motion is identical to that of Placzek *et al.* The flow is simulated for sinusoidal cylinder oscillations of displacement amplitude  $A/d = 0.25$  at frequencies  $f_c/f_s = 0.5, 0.9, 1.1$  and  $1.5$ . For the initial condition, Placzek *et al.* [22] initiated their computations from a stationary cylinder computation at  $Re_d = 100$  in the periodic vortex-shedding flow regime. However, the instant of the vortex shedding cycle at which the computations are initiated is not specified by Placzek *et al.* In the present computations, the initial condition is periodic vortex shedding from a stationary cylinder at  $Re_d = 100$  at the instant when the lift coefficient  $C_L$  is approximately zero.

### 5.2.2. FVPM configuration

The particle distribution in the vicinity of the cylinder is shown in Figure 4. The initial particle spacing is  $\Delta x_0/d \approx 0.36$  in the majority of the domain. This resolution was found sufficient for agreement with reference results. The particle spacing nearest the cylinder is  $\Delta x_s = (0.1)\Delta x_0$  and linearly increases in the radial direction to  $\Delta x_0$  over a distance of  $(5.5)d$  from the cylinder centre. The smoothing length  $h$  is set to 0.7 times the local particle spacing. The particle motion  $\dot{\mathbf{x}}_i$  is determined using a RBF interpolation of the boundary velocities as described in Section 4.

### 5.2.3. Results

As described previously, the forced vibration computations of Placzek *et al.* [22] are used for the purposes of comparison with the FVPM results. In addition, Koopmann [39] presents experimental data for the threshold values of  $A/d$  and  $f_c/f_s$  for which lock-in occurs at Reynolds numbers 100, 200 and 300.

The data presented by Koopmann for  $Re_d = 100$  show that  $f_c/f_s = 0.5$  and  $1.5$  correspond to unlocked behaviour, while  $f_c/f_s = 0.9$  and  $1.1$  correspond to locked behaviour. These observations are used to assess the ability of the FVPM to predict locked or unlocked behaviour at appropriate values of  $f_c/f_s$ .

The maximum lift coefficients for the four different cylinder vibration frequencies are given in Table 1 for both the FVPM and the results of Placzek *et al.* [22]. Good agreement is achieved with the results of Placzek *et al.* [22] for all values of  $f_c/f_s$ .

According to Nobari and Naredan [40] and Placzek *et al.* [22], lock-in for forced vibrations is characterised by a sinusoidal  $C_L$  response and a synchronisation of the  $C_L$  and cylinder vibration frequencies. Figure 5 shows the lift coefficient histories predicted by the FVPM for the four cylinder vibration frequencies at  $Re_d = 100$ . In Figures 5(b) and 5(c) for  $f_c/f_s = 0.9$  and  $1.1$  respectively, the lift coefficient response is sinusoidal, indicating locked behaviour. The prediction of locked behaviour at these values of  $f_c/f_s$  and  $A/d$  is consistent with the experimental observations of Koopmann [39].

Figures 5(a) and 5(d) show the lift coefficient histories for  $f_c/f_s = 0.5$  and  $1.5$  respectively. In these cases,  $C_L(t)$  is no longer sinusoidal, but displays a periodic beating behaviour. This is consistent with unlocked behaviour, and at these values of  $f_c/f_s$  and  $A/d$ , is in agreement with the observations of Koopmann [39].

For  $f_c/f_s = 1.5$  (Figure 5(d)), FVPM correctly predicts the beating behaviour of the transient  $C_L$  response of Placzek *et al.* However, for  $f_c/f_s = 0.5$  (Figure 5(a)) the transient  $C_L$  response predicted by the FVPM differs from the  $C_L$  response of Placzek *et al.* For the time range of  $C_L$  response given in Placzek *et al.* at  $f_c/f_s = 0.5$  the response is not fully periodic but is still settling down from the impulsive start of the cylinder motion. In this non-periodic regime, the  $C_L$  response depends on the initial condition. However, the initial condition employed in the simulations of Placzek *et al.* was not precisely specified — in particular, the instant of the periodic vortex-shedding cycle (in a stationary cylinder simulation) from which the cylinder motion was initiated, was not



given. Hence a meaningful comparison between the transient  $C_L$  response predicted by the FVPM and Placzek *et al.* is not possible in this non-periodic flow regime.

Figure 6 shows the lift coefficient  $C_L(t)$  predicted by FVPM as a function of cylinder displacement  $y(t)/d$  (phase portrait). Figures 6(b) and 6(c) show the phase portraits for  $f_c/f_s = 0.9$  and  $1.1$  respectively. Following an initial asynchronous period due to the impulsive start of the cylinder motion, the lift coefficient oscillations synchronise with those of the cylinder displacement, and the phase portrait settles on a unique path. Figures 6(a) and 6(d) show the phase portraits for  $f_c/f_s = 0.5$  and  $1.5$  respectively. In these figures, asynchronous behaviour between the lift coefficient and cylinder displacement is evident because a unique path is not present in the phase portrait. Comparison with the phase portraits of Placzek *et al.* [22] reveals that the responses predicted by FVPM are similar for  $f_c/f_s = 0.9, 1.1$  and  $1.5$ . For the phase portrait with  $f_c/f_s = 0.5$ , it appears that the  $C_L$  values predicted by the FVPM are the negative of those predicted by Placzek *et al.* One explanation for this behaviour is that the initial conditions in the present simulations may not be identical to those of Placzek *et al.*, as described previously.

### 5.3. Vortex-induced vibration of a cylinder in crossflow

FVPM simulations for VIV of a circular cylinder in crossflow are presented in this section. Throughout this section, the results of Singh and Mittal [36] are used for the purposes of comparison with the FVPM results.

#### 5.3.1. Problem definition

The VIV problem for FVPM validation is defined by Singh and Mittal [36]. The flow domain for the present FVPM simulations is depicted schematically in Figure 7. A circular cylinder of diameter  $d$  is located in a channel of width  $20d$ . Inlet and outlet boundary conditions are prescribed for the vertical boundaries located at  $x^* = x/d = 0$  and  $x^* = 35$  respectively. Free-slip horizontal wall boundary conditions are located at  $y^* = y/d = \pm 10$ . The cylinder centre is

initially located at  $x^* = 10$  and  $y^* = 0$ . The Reynolds number (based on cylinder diameter  $d$  and freestream velocity  $U_\infty$ ) is 100 for all results presented in this section. The cylinder is elastically mounted in both the  $x$  and  $y$  directions with identical structural parameters for each direction. The reduced velocity  $U_r = U_\infty/(f_n d)$  is varied by adjusting the natural frequency  $f_n$  of the structural system while keeping the freestream velocity, and thereby the Reynolds number, fixed. The non-dimensional mass  $M^* = m/(\rho d^2)$  is set to 7.854.

### 5.3.2. Initial conditions

For the majority of the simulations presented in this section, the initial conditions consist of uniform flow with  $x$ -velocity  $U_\infty$  everywhere and zero cylinder velocity, *i.e.*  $\dot{\mathbf{x}}_c = 0$ . This corresponds to the stationary initial condition described in Section 5.1. The  $U_r$  values for the VIV simulations with the stationary initial condition are given in Table 2. In addition, VIV simulations were performed for the case of increasing  $U_r$ . These simulations were initiated by firstly establishing periodic VIV for  $U_r = 7.00$  with the stationary initial condition.  $U_r$  was then sequentially increased in steps, to each of the  $U_r$  values listed in Table 2. Periodic VIV was achieved before increasing the  $U_r$  value. These simulations were performed to assess the ability of the FVPM to predict the effect of the initial condition on the cylinder response. This also facilitated additional comparisons with the results of Singh and Mittal [36], all of whose simulations were performed for increasing  $U_r$ .

### 5.3.3. Particle motion

The particle motion schemes and regions for the present VIV simulations are illustrated schematically in Figure 9. In the FVPM, when the particles move relative to each other, the interaction vectors  $\beta_{ij}$  must be updated. To reduce the computational effort for the present simulations, the particles within a radius  $(5.5)d$  of the cylinder centre move at the same velocity as the cylinder. Thus it is only necessary to compute the interaction vectors for these particles at time  $t = 0$ . Denoting as  $x_c(0)$  the initial cylinder position in the  $x$ -direction, the

motion of the particles located a distance greater than  $(5.5)d$  from the cylinder centre and with  $x$ -coordinates  $x_c(0) - 7d < x < x_c(0) + 7d$  is determined using the RBF interpolation described in Section 4. For the interpolation, the known velocities are those of outer (stationary) boundaries and those of the particles located  $(5.5)d$  from the cylinder centre. All other particles in the domain are fixed.

#### 5.3.4. Particle distribution

As for the forced vibration study, in the majority of the domain, the particles are initially arranged in a uniform Cartesian pattern with spacing  $\Delta x_0$ . The particle spacing decreases over a distance  $(5.5)d$  from the cylinder centre to  $\Delta x_s = \Delta x_0/10$  at the surface.e. The smoothing length for all particles is 0.7 times the initial local particle spacing.

Solution convergence with particle spacing was investigated by conducting simulations at surface particle spacings  $\Delta x_s/d = 0.011, 0.022, 0.044$  at the single physical condition  $U_r = 5.0$ . Results are summarised in Table. 3. According to a Richardson extrapolation [41] of the three data points, the order of convergence is 1.54. The finest resolution,  $\Delta x_s/d = 0.011$ , yields a result within 2.4% of the extrapolated converged result, and the result for  $\Delta x_s/d = 0.022$  is within 7.0%. Therefore, the majority of simulations were conducted with the medium resolution,  $\Delta x_s/d = 0.022$ , resulting in approximately 22,000 particles. This particle distribution is shown in Figure 8.

#### 5.3.5. Results

Results are compared with the moving-mesh finite-element simulations by Singh and Mittal [36] of VIV of a circular cylinder at  $Re_d = 100$  in which the cylinder was elastically mounted in both  $x$  and  $y$  directions. Results are given by Singh and Mittal [36] for the transverse and in-line cylinder displacements and lift and drag coefficients as a function of  $U_r$  for constant  $Re_d$ . Singh and Mittal simulated VIV using a mesh-based finite element scheme with a deforming 2D mesh of 7,236 quadrilateral elements. The simulations of Singh and Mittal were

performed for increasing or decreasing  $U_r$ , not from rest. However, the initial condition only has an effect on the cylinder response for the larger values of  $U_r$  for which lock-in occurs. Therefore the majority of the FVPM results with the stationary initial condition should be comparable with the results of Singh and Mittal. In the following figures, the values from Singh and Mittal are given for increasing  $U_r$  only.

The variation of the maximum non-dimensional amplitude of the transverse cylinder displacement  $y_c/d$  as a function of  $U_r$  is shown in Figure 10 for both the FVPM and reference simulations. Good agreement is achieved with the results of Singh and Mittal, although there are two outlying points at  $U_r = 7.50$  and  $7.75$  for the FVPM simulations with the stationary initial condition. For the case of increasing  $U_r$ , good agreement with the reference is achieved for  $U_r = 7.25$  and  $U_r = 7.5$ . However, for  $U_r = 7.6$  and  $U_r = 7.75$ , FVPM predicts a lower amplitude than the reference solution. FVPM therefore only partially predicts the additional branch in the amplitude response predicted by Singh and Mittal [36] for the case of increasing  $U_r$ . Reasonable agreement between the FVPM and reference values for the root-mean-squared lift coefficient is achieved, as shown in Figure 11.

The non-dimensional cylinder vibration frequency  $f_c/f_n$  is shown in Figure 12 as a function of  $U_r$ . Synchronisation of the cylinder vibration with the natural frequency is evident over the range  $5.0 \lesssim U_r \lesssim 7.0$ . This plot shows the variation of the non-dimensional cylinder vibration frequency  $f_c d/U_\infty$  with  $U_r$  for both FVPM and reference solutions. Also shown is the non-dimensional natural frequency  $f_n d/U_\infty$ . Again, the synchronisation of the cylinder motion and natural frequencies is clear and good agreement is achieved with the results of Singh and Mittal. For the FVPM simulations starting from rest, the frequency response shows a departure from lock-in at lower  $U_r$  values than predicted by Singh and Mittal. For the increasing  $U_r$  case, lock-in is predicted by the FVPM up to  $U_r = 7.5$ , but thereafter the cylinder motion frequency deviates from  $f_n$ , as shown in Figure 12. For the increasing  $U_r$  case, the FVPM thus predicts departure from lock-in at lower  $U_r$  values than Singh and Mittal [36].

In Figure 13, data are plotted alongside results of a highly resolved vortex method for undamped VIV at  $Re_d = 100$  by Shiels *et al.* [38], and the results of Singh and Mittal. Amplitude and frequency are presented as functions of the effective stiffness parameter of Shiels *et al.*,

$$k_{eff} = \frac{k - 4\pi^2 m f_c^2}{\frac{1}{2}\rho U_\infty^2} = 8\pi^2 M^* (f_n^{*2} - f_c^{*2}) , \quad (17)$$

where  $f_c^* = f_c d / U_\infty$  and  $f_n^* = f_n d / U_\infty = 1 / U_r$ . This collapses the effects of structural inertia and stiffness, conventionally characterised by  $M^*$  and  $U_r$ , into a single parameter. However,  $k_{eff}^*$  is unknown *ab initio* for a given configuration, since it depends on the oscillation frequency  $f_c$ . Both the scaling approach and the numerical results of Shiels *et al.* [38] are representative of the only available laminar VIV experiment [32] as well as a range of other numerical results [29].

The present FVPM results agree with computations of Shiels *et al.* [38] for amplitude and frequency. The maximum discrepancy in amplitude is consistent with the 7% error predicted by Richardson extrapolation, and in most cases it is smaller. Discrepancies between the present work and Singh and Mittal (most clearly visible in Figure 10) occur at the lowest oscillation frequencies, in the region  $-0.36 < k_{eff}^* < 0.01$  and  $f_c^* < 0.13$ . In this region, FVPM agrees well with Shiels *et al.*, whereas the results of Singh and Mittal predict lower oscillation frequency.

The temporal variation of  $y_c/d$  for various  $U_r$  values is shown in Figures 14, 15 and 16. The amplitude of the  $y_c/d$  response is greater than 0.3 and the motion is sinusoidal for  $U_r = 5.25, 6.25$  and  $7.00$  as shown in Figures 14(b), 15(a) and 15(b) respectively. Starting from rest with  $U_r = 7.50$ , the cylinder motion is characterised by a smaller amplitude and a beating behaviour in which the motion is periodic over several non-periodic oscillations, as shown in Figure 16(a). For the increasing  $U_r$  case at  $U_r = 7.50$  (Figure 16(b)), the transient  $y_c/d$  response is quite different than for the stationary initial condition case — the motion is sinusoidal and the amplitude of the motion is larger.

The temporal variation of the lift coefficient is shown in Figures 17, 18 and 19 for different  $U_r$  values. For  $U_r = 4.40$  and  $5.25$  (Figure 17), the lift coefficient

response is sinusoidal with  $\max(C_L) = 0.6$  and  $0.9$  respectively. The amplitude of the  $C_L$  variation for these  $U_r$  values is much larger than for flow over a stationary cylinder at  $Re_d = 100$  in the periodic vortex shedding regime, for which  $\max(C_L) = 0.36$ . In Figure 18 the transient  $C_L$  response is shown for  $U_r = 6.25$  and  $7.00$ . In both of these cases, transient  $C_L$  response is periodic with several non-periodic oscillations within each period and is characterised by sudden sharp variations. For  $U_r = 7.50$  with the stationary initial condition (Figure 19(a)), the response is again periodic over several oscillations, but the sharp variations are no longer apparent. For the increasing  $U_r$  case, shown in Figure 19(b), the  $C_L$  response is purely sinusoidal but with a slightly smaller amplitude than for the stationary initial condition.

The  $z$ -component of the vorticity is given by

$$\zeta_z = \frac{\partial v}{\partial x} - \frac{\partial u}{\partial y}, \quad (18)$$

which may be computed using the FVPM approximation

$$\zeta_z = \frac{1}{V_i} \sum_{j=1}^N \left( \beta_{ij}^{(x)} \frac{v_i + v_j}{2} - \beta_{ij}^{(y)} \frac{u_i + u_j}{2} \right), \quad (19)$$

where  $\beta_{ij}^{(x)}$  and  $\beta_{ij}^{(y)}$  denote the  $x$  and  $y$  components of the particle interaction vector, respectively. Figure 20 shows the instantaneous non-dimensional vorticity field  $\zeta_z d/U_\infty$ , computed using Eq. (19), for  $U_r = 4.40$ ,  $5.00$  and  $6.25$ . For  $U_r = 4.40$  and  $6.25$ , two vortices are shed from the cylinder per cycle. This mode of vortex shedding is denoted by Williamson and Roshko [34] as the 2S mode and is the predominant mode that exists for laminar flow over vibrating circular cylinders. For  $U_r = 5.00$ , two vortices are also shed per cycle, but the shed vortices coalesce with downstream vortices of the same rotational direction. This prediction of the C(2S) vortex shedding mode is consistent with the results of Singh and Mittal [36].

## 6. Discussion and conclusions

FVPM has been extended to rigid-body FSI modelling, using a staggered algorithm for the fluid-structure coupling, with arbitrary Lagrange-Euler particle

motion. FVPM for flow about a body with prescribed motion was first validated for forced vibrations of a circular cylinder in crossflow. This test was performed to assess the ability of the FVPM to predict the lock-in phenomenon associated with flow over vibrating cylinders. The developed extension was then validated for VIV of a rigid circular cylinder in a crossflow at  $Re_d = 100$ . The validation was performed on the basis of the structure displacements and lift coefficients. For these parameters, good agreement was achieved between the FVPM results and reference numerical solutions. Furthermore, the FVPM correctly predicted the different wake patterns associated with different structural parameters.

Four aspects of both the basic FVPM and the extensions described in this article are critical for the accurate simulation of the chosen validation problems. Firstly, the scheme can predict the pressure field accurately. Secondly, due to the precise definition of boundary terms in the discrete FVPM scheme, it is straightforward to compute the total fluid force on the structure by integrating the pressure field over the boundary. Thirdly, the motion of the structure and flow field are coupled by an appropriate temporal algorithm as described in this article. Finally, the present choice of particle motion scheme allows a high spatial resolution to be maintained near the structure boundary for the duration of the simulation. The results presented in this article demonstrate the accuracy of the developed FSI extension of the FVPM and show that the method is a robust tool for meshless simulation of FSI problems. More generally, this study confirms that meshless methods may be used for accurate prediction of large body motions in flow.

The moving-body problems studied here have been successfully modelled using mesh-based numerical methods (as the problems were selected to facilitate comparison with other results.) However, in principle, the meshless FVPM method can handle arbitrarily large or complex body motions (such as rigid-body rotations and multiple bodies) which may be beyond the capability of schemes based on mesh deformation.

It remains to improve the computational efficiency of FVPM, in particular for 3D simulations. In 2D, the calculation of particle interaction vectors is by

far the most costly part of the algorithm, and in 3D it is prohibitive. In future work, faster alternative methods will be investigated.

## 7. Acknowledgements

The authors gratefully acknowledge the support of the European Community's Seventh Framework Programme (FP7/2007-2013) under grant agreement 225967 NextMuSE. Ruairi Nestor was supported by an IRCSET Government of Ireland Postgraduate Scholarship.

## References

- [1] J. Monaghan, Simulating free surface flows with SPH, *Journal of Computational Physics* 110 (1994) 399–406.
- [2] S. Cummins, M. Rudman, An SPH projection method, *Journal of Computational Physics* 152 (1999) 584–607.
- [3] S. Shao, E. Lo, Incompressible sph method for simulating newtonian and non-newtonian flows with a free surface, *Advances in Water Resources* 26 (7) (2003) 787–800.
- [4] J. Monaghan, Smoothed particle hydrodynamics and its diverse applications, *Annual Review of Fluid Mechanics* 44 (2012) 323–346.
- [5] D. Hietel, K. Steiner, J. Struckmeier, A finite volume particle method for compressible flows, *Mathematical Models and Methods in Applied Sciences* 10 (2000) 1363–1382.
- [6] M. Junk, J. Struckmeier, Consistency analysis of meshfree methods for conservation laws, *Mitteilungen der Gesellschaft für Angewandte Mathematik und Mechanik* 24 (2001) 99–126.
- [7] M. Junk, Do finite volume methods need a mesh?, *Lecture Notes in Computational Science and Engineering*, Springer, 2003, pp. 223–238.



- [8] R. Keck, D. Hietel, A projection technique for incompressible flow in the meshless finite volume particle method, *Advances in Computational Mathematics* 23 (2005) 143–169.
- [9] D. Hietel, R. Keck, Consistency by coefficient correction in the finite volume particle method, in: M. Griebel (Ed.), *Meshfree Methods for Partial Differential Equations, Lecture Notes in Computational Science and Engineering*, Springer, Berlin, 2003, pp. 211–221.
- [10] D. Teleaga, A finite volume particle method for conservation laws, Ph.D. thesis, University of Kaiserslautern (2005).
- [11] R. M. Nestor, M. Basa, M. Lastiwka, N. J. Quinlan, Extension of the finite volume particle method to viscous flow, *Journal of Computational Physics* 228 (2009) 1733–1749.
- [12] D. Teleaga, J. Struckmeier, A finite-volume particle method for conservation laws on moving domains, *International Journal for Numerical Methods in Fluids* 58 (2008) 945–967.
- [13] R. M. Nestor, N. J. Quinlan, Incompressible moving-boundary flows with the finite volume particle method, *Computer Methods in Applied Mechanics and Engineering* 199 (2010) 2249–2260.
- [14] J. Bonet, T.-S. Lok, Variational and momentum preservation aspects of smooth particle hydrodynamic formulations, *Computer Methods in Applied Mechanics and Engineering* 180 (1999) 97–115.
- [15] A. Harten, P. Lax, B. van Leer, On upstream differencing and Godunov-type schemes for hyperbolic conservation laws, *SIAM Review* 25 (1983) 35–61.
- [16] R. Keck, The finite volume particle method: A meshless projection method for incompressible flow, Ph.D. thesis, University of Kaiserslautern (2002).

- [17] A. Chorin, Numerical solution of the Navier-Stokes equations, *Mathematics of Computation* 22 (1968) 745–762.
- [18] T. Skalicky, Laspack 1.12.2, Online: <http://dddas.org/mgnet/Codes/laspack/html/laspack.html> (1995).
- [19] J. Ferziger, M. Peric, *Computational Methods for Fluid Dynamics*, Springer, Berlin, 2002.
- [20] J. Zhang, C. Dalton, Interactions of vortex-induced vibrations of a circular cylinder and a steady approach flow at a Reynolds number of 13,000, *Computers & Fluids* 25 (1996) 283–294.
- [21] C. Farhat, M. Lesoinne, Two efficient staggered algorithms for the serial and parallel solution of three-dimensional nonlinear aeroelastic problems, *Computer Methods for Applied Mechanics and Engineering* 182 (2000) 13–22.
- [22] A. Placzek, J. Sigrist, A. Hamdouni, Numerical simulation of an oscillating cylinder in a cross-flow at low Reynolds number: Forced and free oscillations, *Computers & Fluids* 38 (2009) 80–100.
- [23] A. de Boer, M. van der Schoot, H. Bijl, Mesh deformation based on radial basis function interpolation, *Computers & Structures* 85 (2007) 784–795.
- [24] M. Buhmann, *Radial Basis Functions: Theory and Implementations*, Cambridge University Press, Cambridge, 2003.
- [25] Y. Saad, M. Schultz, GMRES: A generalized minimal residual algorithm for solving nonsymmetric linear systems, *SIAM Journal of Scientific and Statistical Computing* 7 (1986) 856–869.
- [26] P. Bearman, Vortex shedding from oscillating bluff bodies, *Annual Review of Fluid Mechanics* 16 (1984) 195–222.

- [27] C. Le Cunff, F. Biolley, E. Fontaine, S. Etienne, M. Facchinetti, Vortex-induced vibrations of risers: theoretical, numerical and experimental investigation, *Oil & Gas Science and Technology* 57 (2002) 59–69.
- [28] J. Cermak, Aerodynamics of buildings, *Annual Review of Fluid Mechanics* 8 (1976) 75–106.
- [29] C. Williamson, R. Govardhan, Vortex-induced vibrations, *Annual Review of Fluid Mechanics* 36 (2004) 413–455.
- [30] T. Sarpkaya, A critical review of the intrinsic nature of vortex-induced vibrations, *Journal of Fluids and Structures* 19 (2004) 389–447.
- [31] D. Newman, G. Karniadakis, Simulations of flow over a flexible cable: A comparison of forced and flow-induced vibration, *Journal of Fluids and Structures* 10 (1996) 439–453.
- [32] P. Anagnostopoulos, P. Bearman, Response characteristics of a vortex-excited cylinder at low Reynolds numbers, *Journal of Fluids and Structures* 6 (1992) 39–50.
- [33] A. Khalak, C. Williamson, Motions, forces and mode transitions in vortex-induced vibrations at low mass-damping, *Journal of Fluids and Structures* 13 (1999) 813–851.
- [34] C. Williamson, A. Roshko, Vortex formation in the wake of an oscillating cylinder, *Journal of Fluids and Structures* 2 (1988) 355–381.
- [35] O. Griffin, S. Ramberg, The vortex-street wakes of vibrating cylinders, *Journal of Fluid Mechanics* 66 (1974) 553–576.
- [36] S. Singh, S. Mittal, Vortex-induced oscillations at low Reynolds numbers: Hysteresis and vortex-shedding modes, *Journal of Fluids and Structures* 20 (2005) 1085–1104.
- [37] T. K. Prasanth, S. Mittal, Vortex-induced vibrations of a circular cylinder at low Reynolds numbers, *Journal of Fluid Mechanics* 594 (2008) 463–491.

- [38] D. Shiels, A. Leonard, A. Roshko, Flow-induced vibration of a circular cylinder at limiting structural parameters, *Journal of Fluids and Structures* 15 (1) (2001) 3–21. doi:10.1006/jfls.2000.0330.  
URL <http://dx.doi.org/10.1006/jfls.2000.0330>
- [39] G. Koopmann, The vortex wakes of vibrating cylinders at low Reynolds numbers, *Journal of Fluid Mechanics* 28 (1967) 501–512.
- [40] M. Nobari, H. Naderan, A numerical study of flow past a cylinder with cross flow and inline oscillation, *Computers & Fluids* 35 (2006) 393–415.
- [41] P. J. Roache, *Verification and Validation in computational science and engineering*, Hermosa, Albuquerque, 1998.

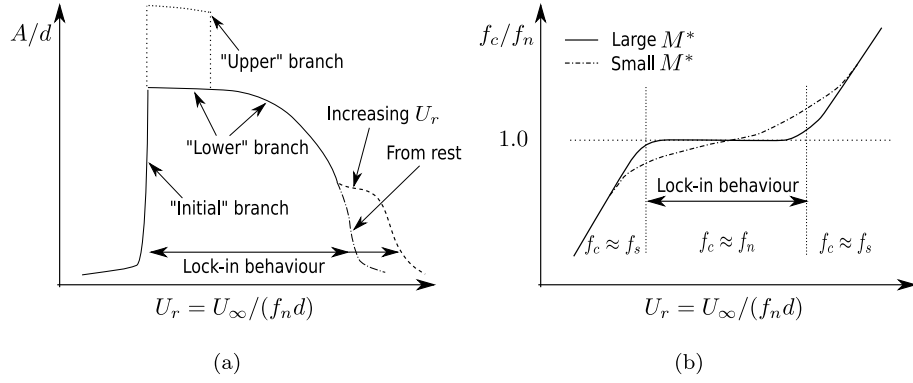


Figure 1: Schematic diagram illustrating the VIV response of (a) the cylinder displacement amplitude  $A/d$  and (b) the cylinder vibration frequency  $f_c/f_n$  as a function of the reduced velocity  $U_r = U_\infty/(f_n d)$ .

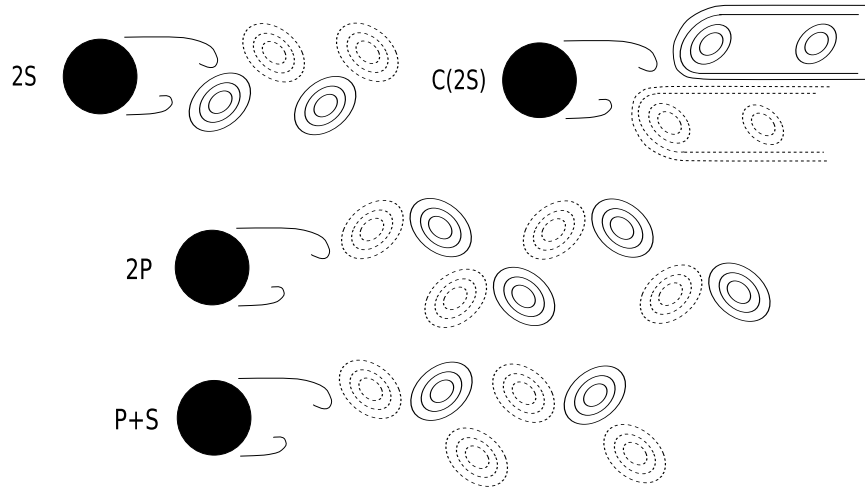


Figure 2: Schematic diagram illustrating the vortex modes in the wake of a forced or freely-vibrating circular cylinder and associated nomenclature. Solid and dashed lines are contours of positive and negative vorticity respectively.

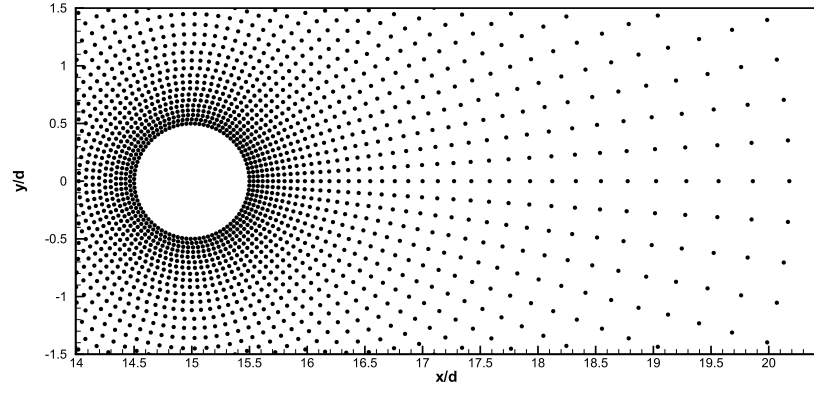


Figure 4: Initial particle distribution for forced vibrations of a circular cylinder in crossflow.

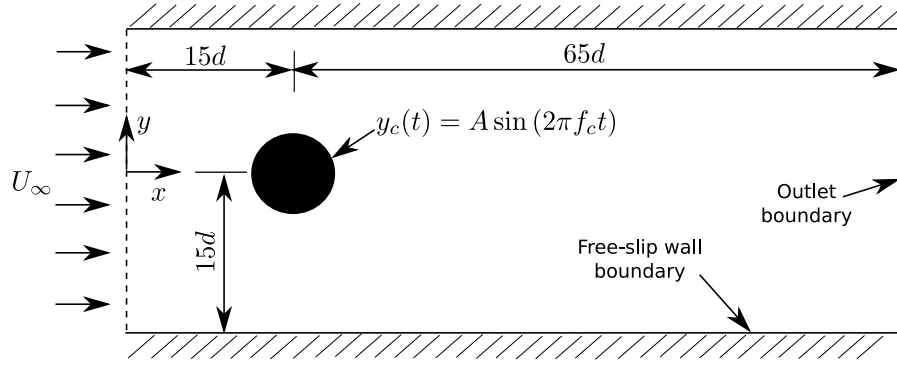


Figure 3: Schematic diagram depicting the flow domain and boundary conditions for forced vibrations of a circular cylinder in crossflow (not to scale).

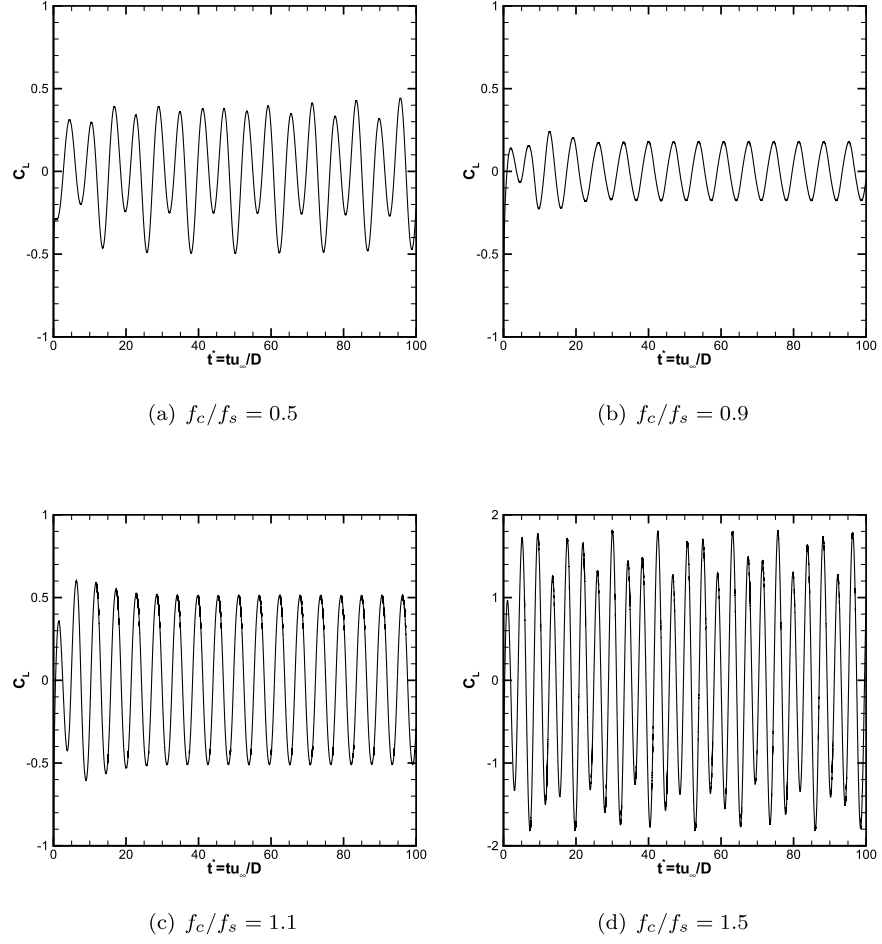


Figure 5: Lift coefficient histories predicted by the FVPM for forced cylinder vibrations at  $Re_d = 100$  with amplitude  $A/d = 0.25$ . Results are shown for different non-dimensional cylinder vibration frequencies  $f_c/f_s$ .

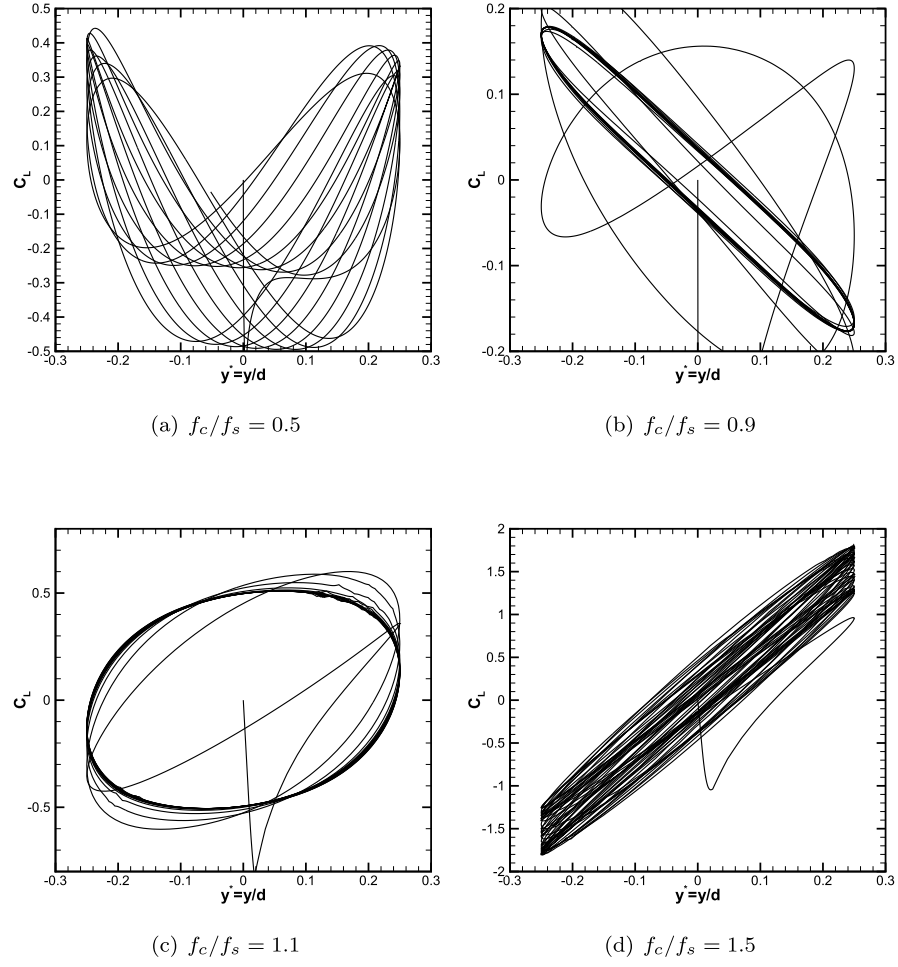


Figure 6: Forced cylinder vibration phase portraits predicted by the FVPM at  $Re_d = 100$  with amplitude  $A/d = 0.25$ . Results are shown for different non-dimensional cylinder vibration frequencies  $f_c/f_s$ .



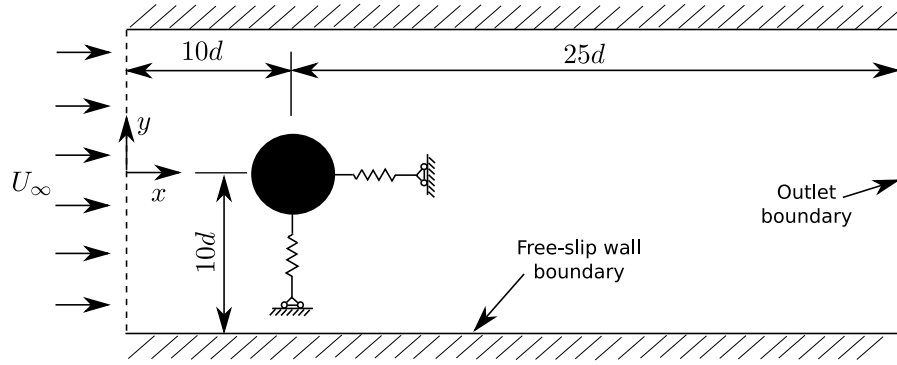


Figure 7: Schematic diagram depicting the flow domain and boundary conditions for VIV of an elastically mounted circular cylinder (not to scale).

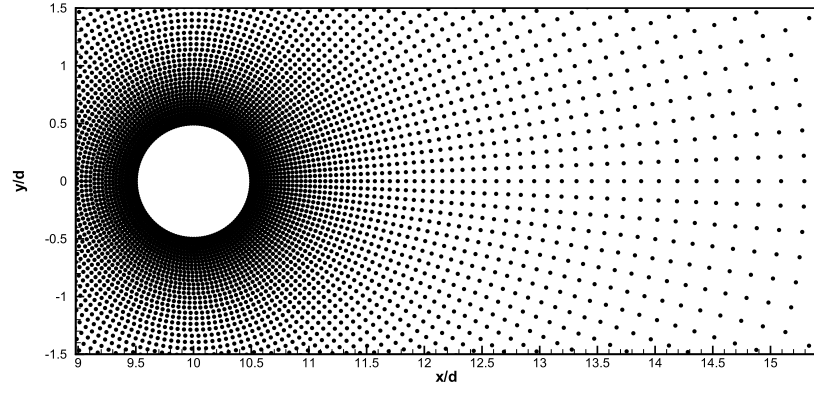


Figure 8: Initial particle distribution for VIV of a circular cylinder in crossflow.

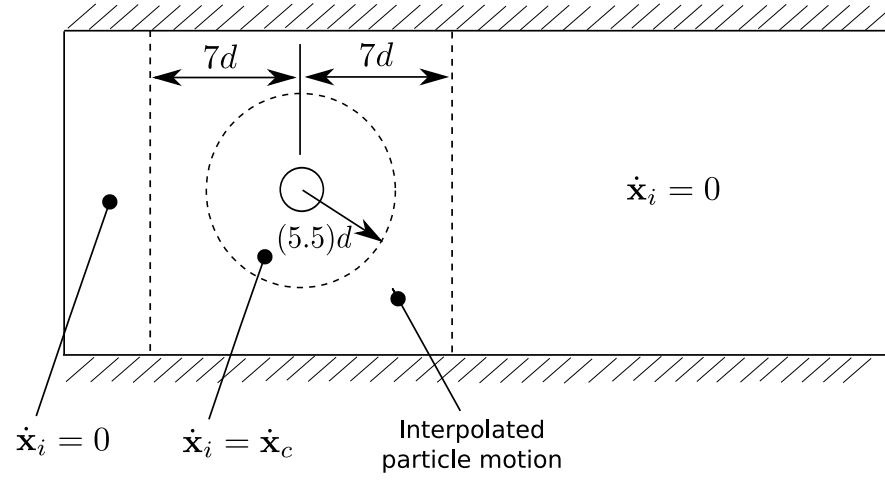


Figure 9: Schematic diagram depicting the regions in which different schemes for the particle motion  $\dot{\mathbf{x}}_i$  are employed for the FVPM simulation of VIV of a circular cylinder.

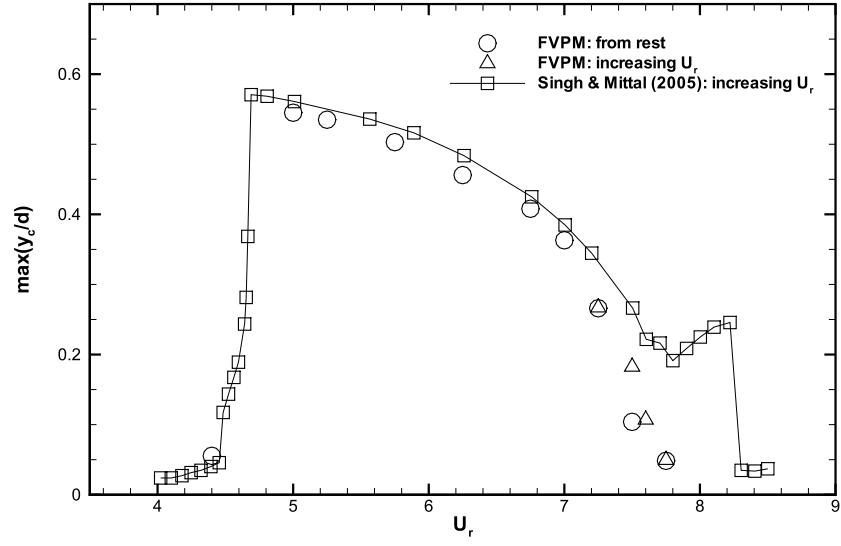


Figure 10: Variation of maximum non-dimensional transverse cylinder displacement  $\max(y_c)/d$  with the reduced velocity  $U_r$  for VIV of a circular cylinder at  $Re_d = 100$ . Comparison between FVPM and the results of Singh and Mittal [36].

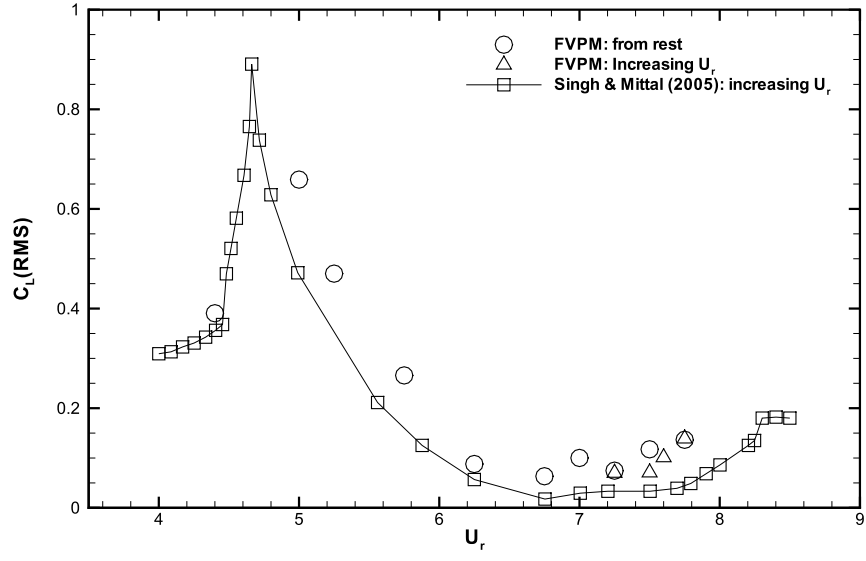


Figure 11: Variation of root mean squared lift coefficient  $C_L$  with reduced velocity  $U_r$  for VIV of a circular cylinder at  $Re_d = 100$ . Comparison between FVPM and the results of Singh and Mittal [36].

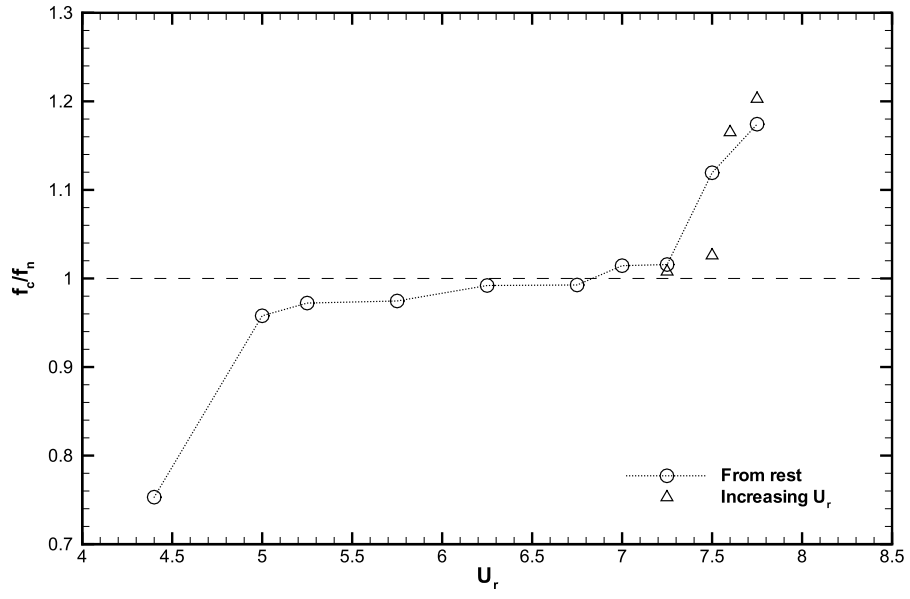


Figure 12: Variation of non-dimensional transverse cylinder vibration frequency  $f_c/f_n$  with reduced velocity  $U_r$  predicted by the FVPM for VIV of a circular cylinder at  $Re_d = 100$ .

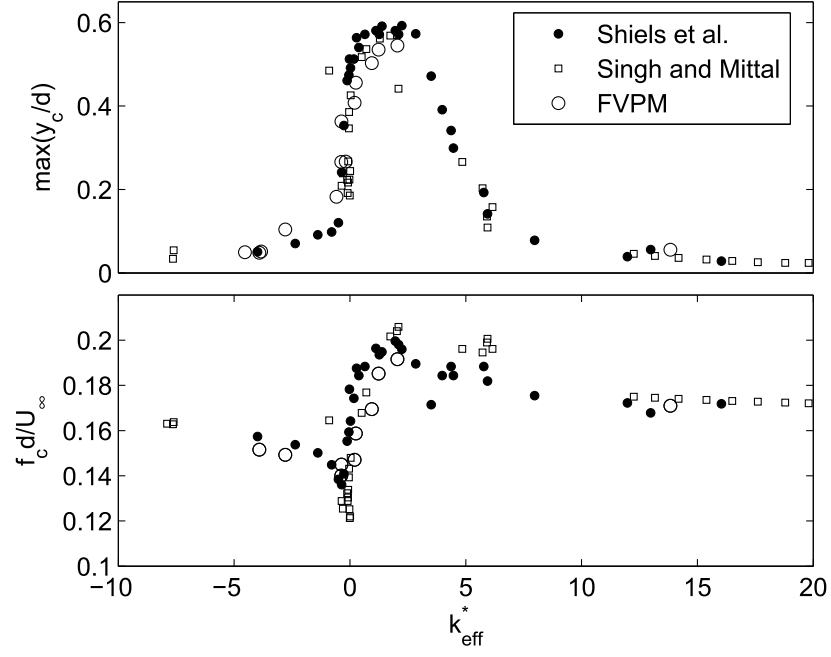
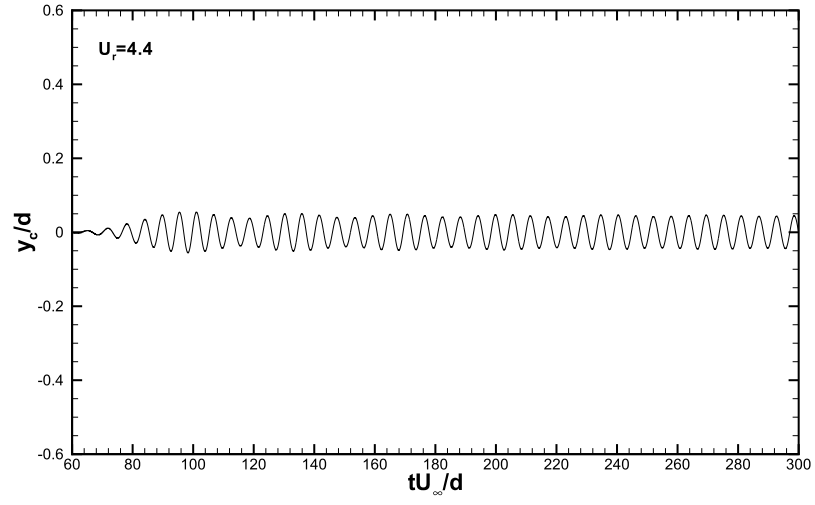
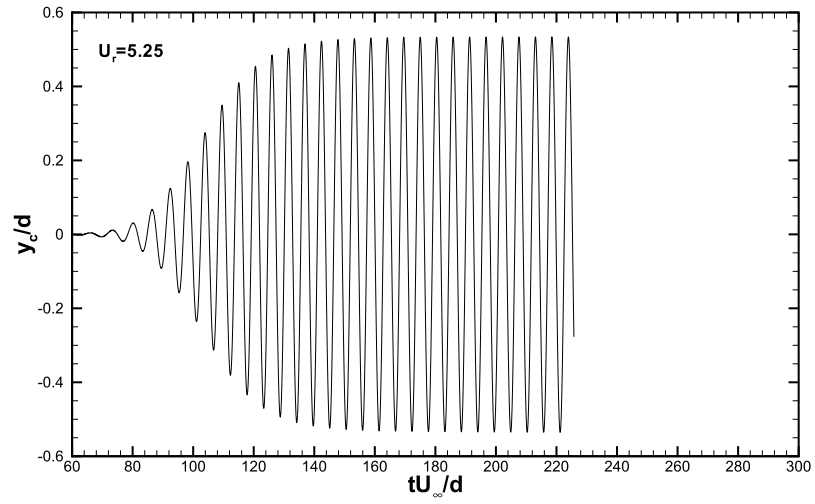


Figure 13: Variation of maximum non-dimensional transverse cylinder displacement  $\max(y_c)/d$  and non-dimensional transverse cylinder vibration frequency  $f_c d/U_\infty$  with the effective stiffness parameter  $k_{eff}^*$  of Shields *et al.* [38]. Comparison between FVPM, Singh and Mittal [36] and Shields *et al.* [38]

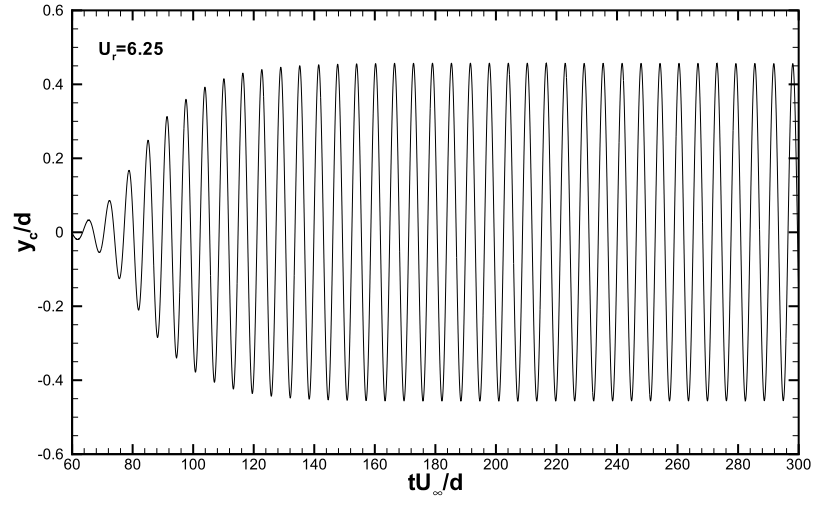


(a)

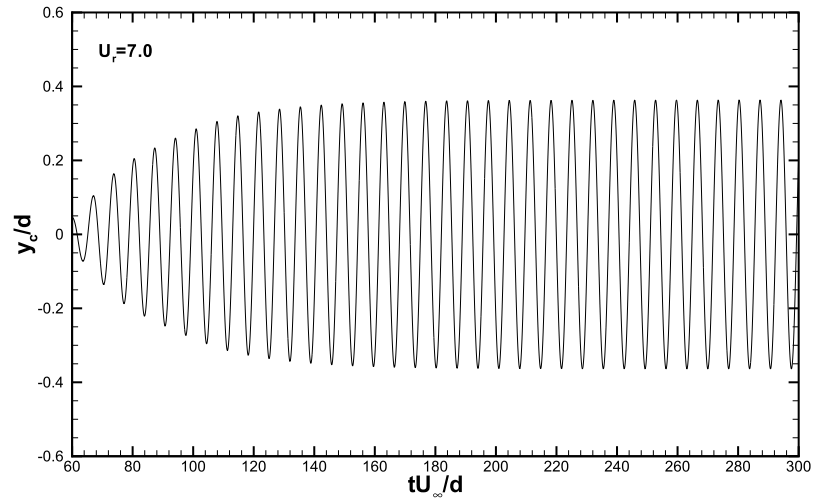


(b)

Figure 14: Transverse cylinder displacement histories predicted by the FVPM for VIV of a circular cylinder at  $Re_d = 100$  and  $U_r = 4.40$  and  $5.25$ . The cylinder is initially at rest.



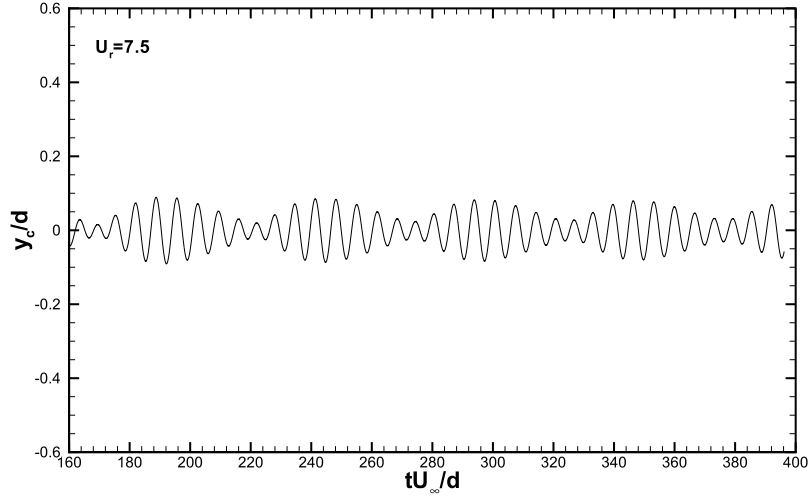
(a)



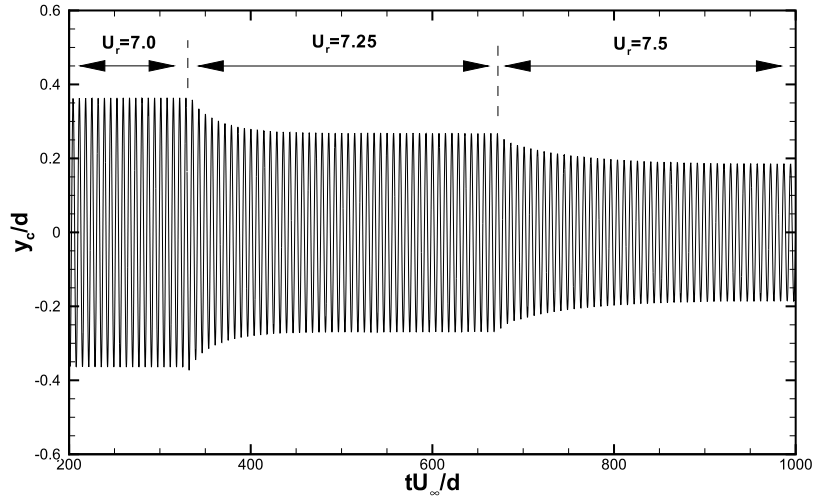
(b)

Figure 15: Transverse cylinder displacement histories predicted by the FVPM for VIV of a circular cylinder at  $Re_d = 100$  and  $U_r = 6.25$  and  $7.00$ . The cylinder is initially at rest.



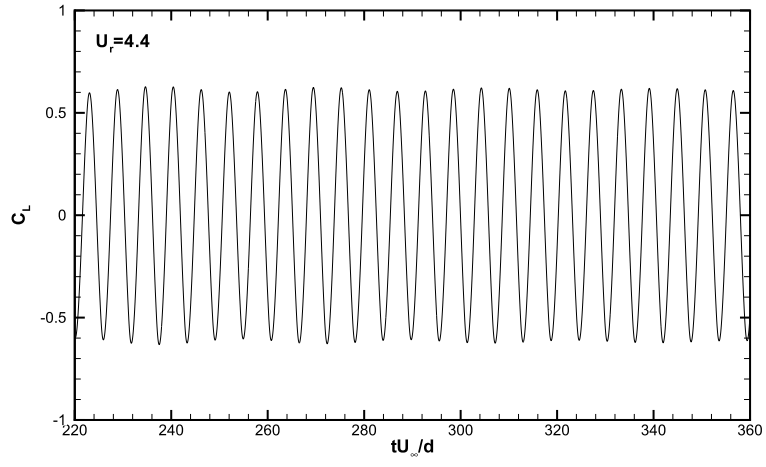


(a)

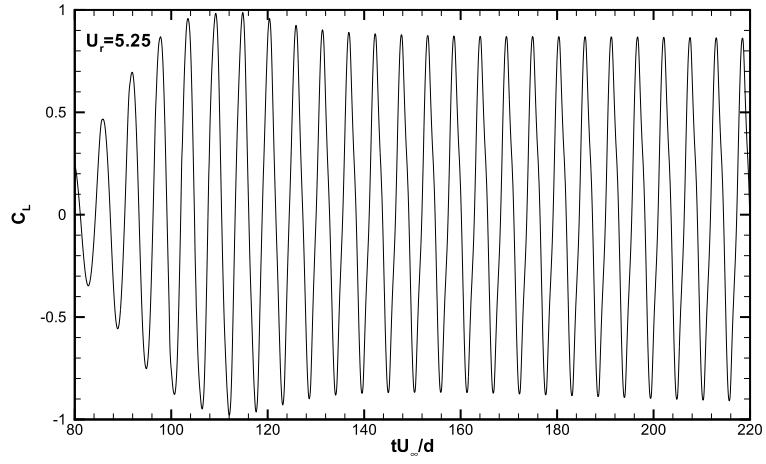


(b)

Figure 16: Transverse cylinder displacement histories predicted by the FVPM for VIV of a circular cylinder at  $Re_d = 100$  at  $U_r = 7.50$ . (a) Cylinder initially at rest, (b)  $U_r$  increasing in steps from 7.00 to 7.25 to 7.50.

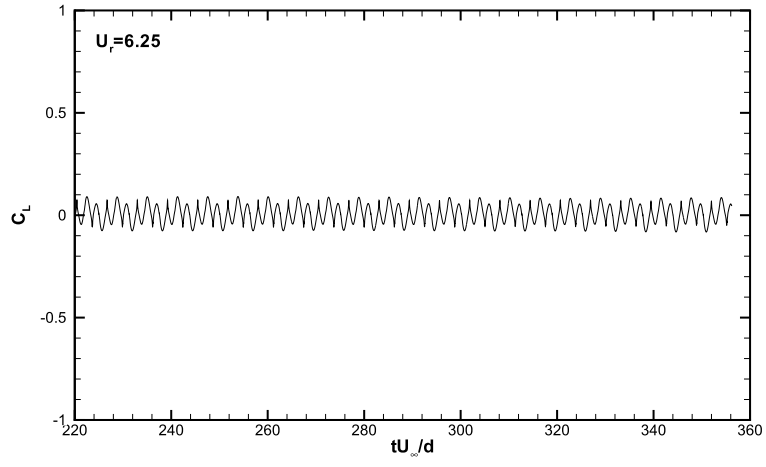


(a)

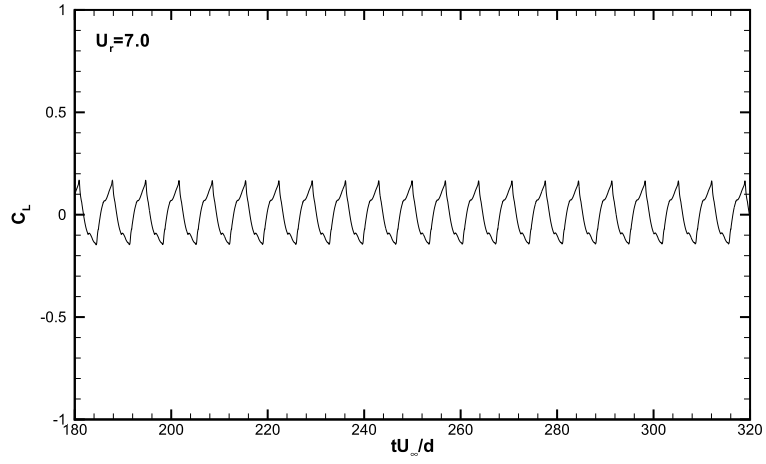


(b)

Figure 17: Lift coefficient histories predicted by the FVPM for VIV of a circular cylinder at  $Re_d = 100$  and  $U_r = 4.40$  and  $5.25$ . The cylinder is initially at rest.

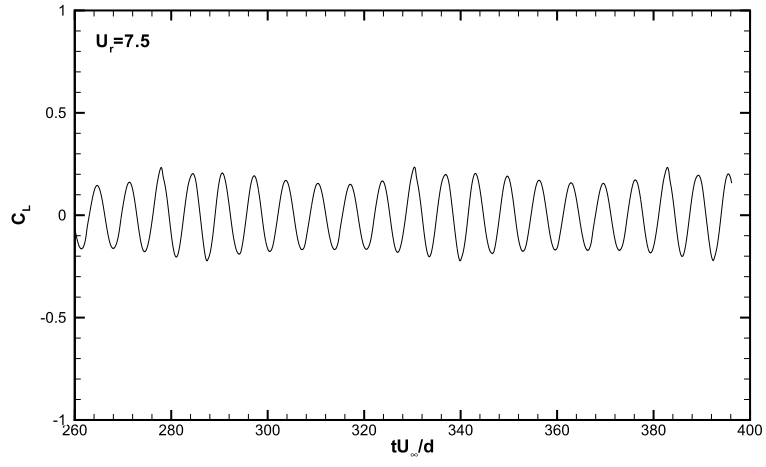


(a)

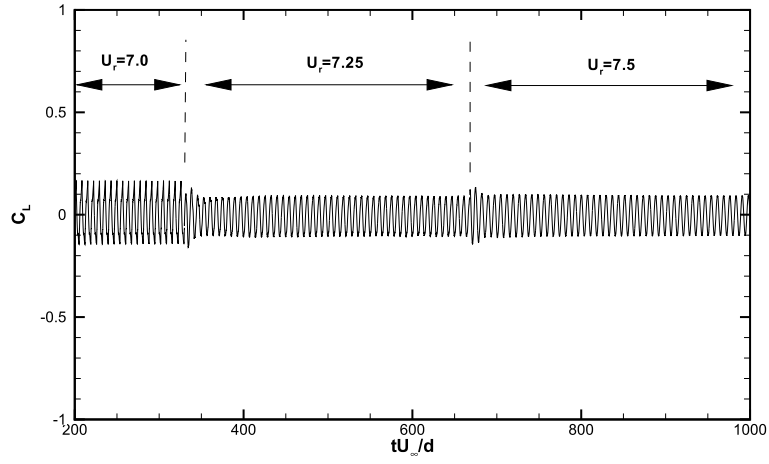


(b)

Figure 18: Lift coefficient histories predicted by the FVPM for VIV of a circular cylinder at  $Re_d = 100$  and  $U_r = 6.25$  and  $7.00$ . The cylinder is initially at rest.

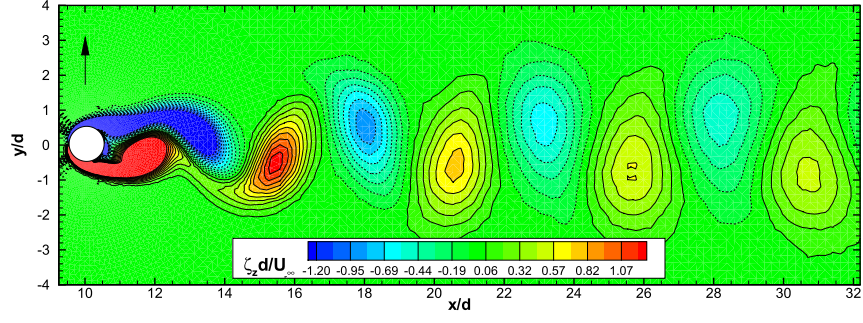


(a)

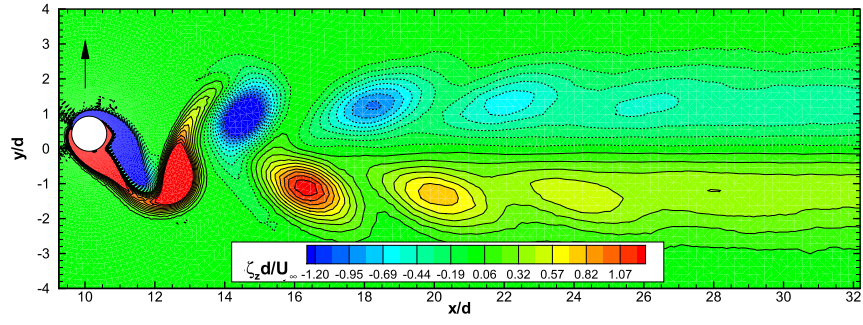


(b)

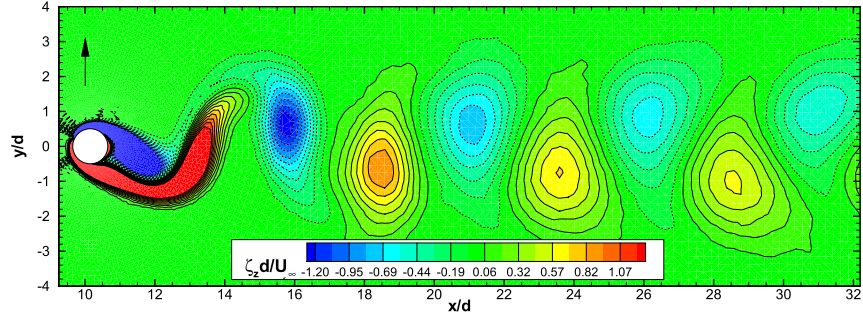
Figure 19: Lift coefficient histories predicted by the FVPM for VIV of a circular cylinder at  $Re_d = 100$  and  $U_r = 7.50$ . (a) Cylinder initially at rest, (b)  $U_r$  increasing in steps from 7.00 to 7.25 to 7.50.



(a)  $U_r = 4.40$ ,  $t^* = 366$



(b)  $U_r = 5.00$ ,  $t^* = 222$



(c)  $U_r = 6.25$ ,  $t^* = 352$

Figure 20: Instantaneous non-dimensional vorticity fields predicted by the FVPM for VIV of a circular cylinder at  $Re_d = 100$  and  $U_r = 4.4$ ,  $5.00$  and  $6.25$ . The arrow indicates the instantaneous direction of the transverse cylinder motion.

Table 1: Maximum lift coefficients for forced vibration of a circular cylinder in crossflow at  $Re_d = 100$  with amplitude  $A/d = 0.25$  for both the FVPM and the simulations of Placzek *et al.* [22]. Results are shown for four non-dimensional cylinder vibration frequencies  $f_c/f_s$ .

$f_c/f_s$	$\max(C_L(t))$			
	0.5	0.9	1.1	1.5
Placzek <i>et al.</i> [22]	0.42	0.15	0.52	1.95
FVPM	0.44	0.18	0.51	1.80

Table 2:  $U_r$  values for which VIV simulations were performed.  $U_r$  values are given for the stationary and increasing  $U_r$  initial conditions.

$U_r$										
Stationary	4.40	5.00	5.25	5.75	6.25	6.75	7.00	7.25	7.50	7.75
Increasing $U_r$	7.25	7.50	7.60	7.75						

Table 3: Maximum transverse oscillation amplitude,  $y_{max}/d$ , computed on various spatial resolution and by Richardson extrapolation.

$\Delta x_s/d$	$y_{max}/d$
0.044	0.4495
0.022	0.5260
0.011	0.5522
extrapolated	0.5658

---

**Algorithm 1** One timestep in the incompressible FVPM with FSI

---

- 1: Compute approximate fluid velocity:  $\mathbf{u}_i^{n+1,*} = \mathbf{u}_i^n + \Delta t (d\mathbf{u}/dt)_i^n$ .
- 2: Update particle positions:  $\mathbf{x}_i^{n+1} = \mathbf{x}_i^n + \Delta t \dot{\mathbf{x}}_i^n$ .
- 3: Update structure displacement and velocity:

$$\begin{aligned}\ddot{\mathbf{x}}_c^n &= \mathbf{F}_f^n/m - 4\pi^2 f_n \mathbf{x}_c^n \\ \dot{\mathbf{x}}_c^{n+1} &= \dot{\mathbf{x}}_c^n + \Delta t \ddot{\mathbf{x}}_c^n \\ \mathbf{x}_c^{n+1} &= \mathbf{x}_c^n + \Delta t \dot{\mathbf{x}}_c^n.\end{aligned}$$

- 4: Set boundary conditions.
- 5: Search for particle neighbours.
- 6: Set particle velocity  $\dot{\mathbf{x}}_i^{n+1}$ .
- 7: Compute  $\beta_{ij}^{n+1}$  and  $\mathbf{b}_i^{n+1}$ .
- 8: Solve for fluid pressure  $p_i^{n+1}$  and update fluid velocity to  $\mathbf{u}_i^{n+1}$ :

$$\begin{aligned}\nabla^2 p_i^{n+1} &= (\rho/\Delta t) \nabla \cdot \mathbf{u}_i^{n+1,*} \\ \mathbf{u}_i^{n+1} &= \mathbf{u}_i^{n+1,*} - (\Delta t/\rho) \nabla p_i^{n+1}.\end{aligned}$$

- 9:  $n = n + 1$ , repeat.
-